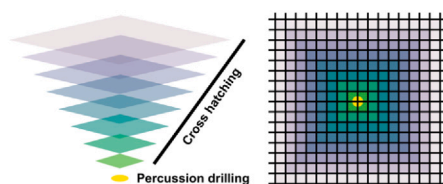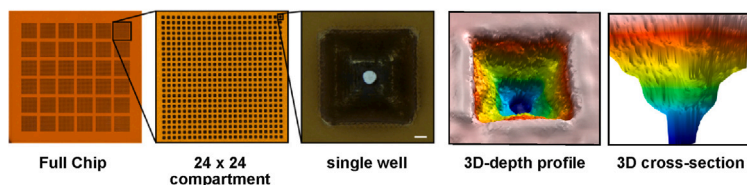**Article**

A systematic comparison of Kapton-based HARE chips for fixed-target serial crystallography
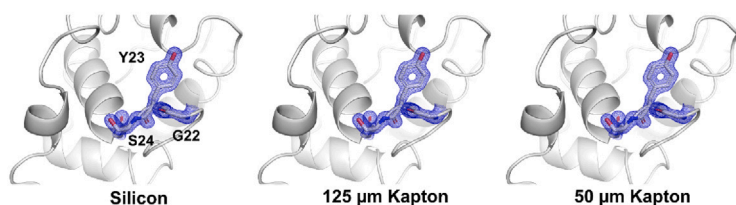

- **Laser ablation of pyramidal shaped wells**

  Cross hatching
  Percussion drilling

- **HARE pattern kapton chips**

  Full Chip | 24 x 24 compartment | single well | 3D-depth profile | 3D cross-section

- **Serial crystallography systematic comparison**

  Y23
  S24 G22

  Silicon | 125 µm Kapton | 50 µm Kapton

HARE serial crystallography chips display a versatile and efficient sample delivery platform and are typically made of silicon. Bosman et al. systematically compare serial crystallography experiments on five different proteins, suggesting Kapton as a cost-effective alternative to silicon as a support material for serial crystallography chips.

Robert Bosman, Andreas Prester, Sihyun Sung, ..., Matthias Wilmanns, Martin Osbild, Eike C. Schulz

ec.schulz@uke.de

Highlights

Micrometer-precision polymer laser drilling of pyramid-shaped features

Full-size HARE pattern polymer serial crystallography sample holder

Systematic chip and data quality comparison across 15 protein crystal structures

Article

A systematic comparison of Kapton-based HARE chips for fixed-target serial crystallography

Robert Bosman,[1] Andreas Prester,[1] Sihyun Sung,[2] Lea von Soosten,[1] Stella Dibenedetto,[1] Kim Bartels,[1] David von Stetten,[2] Pedram Mehrabi,[3,4] Marc Blatter,[5] Gang Lu,[5] Bernhard Suer,[5] Matthias Wilmanns,[1,2] Martin Osbild,[6] and Eike C. Schulz[1,3,4,7,*]

SUMMARY

Fixed targets are a versatile sample delivery method for serial crystallography experiments and a favorable choice regarding sample efficiency. The hit-and-return (HARE) chips utilize pyramidal-shaped features to pre-position crystals in a regular pattern. Typically, these micron-sized features are chemically etched into single-crystal silicon wafers providing a rigid sample mount with minimal background. As polymer chips are emerging as an alternative, here we report the production of HARE chips identical to silicon with pyramidal-shaped features and micron accuracy by laser ablating Kapton foils. We systematically compare the serial crystallography experiments of five different proteins using both Kapton and silicon HARE chips. Comparing these 15 structures, Kapton HARE chips yield data quality that is comparable to the silicon chips. Therefore, we propose that Kapton is a viable and cost-effective alternative support material.

INTRODUCTION

Serial synchrotron crystallography (SSX) is an emergent technique in protein crystallography where reflection intensities are measured from thousands of individual crystals at random orientations.[1–3] Initially developed for use at X-ray free-electron lasers where high-brilliance pulses destroy the crystals precluding sample rotation, SSX has been successfully adapted to microfocus beamlines at third- and fourth-generation synchrotrons.[4,5] As only a single (or very few) diffraction images are recorded from each crystal, radiation damage is minimal, and measurements can be carried out at ambient temperatures.[6,7] More recent developments also extend this to physiologically relevant temperatures.[8] The serial collection scheme permits time-resolved studies on irreversible reactions such as substrate binding, catalysis, light triggering, or other perturbations, which can be performed to each crystal individually before X-ray exposure. Recent hardware, timing, and data-processing developments have permitted time-resolved SSX (TR-SSX) to generate important insights into protein dynamics,[9] substrate binding, and enzyme catalysis.[10,11] Several methodologies have emerged to replace crystals in the beam for each exposure such as liquid jets,[12] lipidic cubic phase (LCP) extruders, drop-on-tape (DoT),[13] and fixed targets.[1,14] DoT and fixed targets place the crystals onto a solid support structure, which brings the crystals into the beam. For DoT, picoliter to nanoliter droplets are ejected onto a moving conveyor belt, which runs past the beam position. Fixed-target approaches place crystals onto a support, which is placed orthogonal to the X-ray beam and then rastered across the beam. This permits strategies to pre-position the crystals, which increases crystal hits while

[1]University Medical Center Hamburg-Eppendorf (UKE), Martinistr. 52, 20246 Hamburg, Germany

[2]European Molecular Biology Laboratory (EMBL), Hamburg Unit, Notkestr. 85, 22761 Hamburg, Germany

[3]Max-Planck-Institute for Structure and Dynamics of Matter, Luruper Chaussee 149, 22761 Hamburg, Germany

[4]Institute for Nanostructure and Solid State Physics, Universität Hamburg, Luruper Chaussee 149, 22761 Hamburg, Germany

[5]RWTH Aachen University, Templergraben 55, 52062 Aachen, Germany

[6]Fraunhofer Institute for Laser Technology ILT, Steinbachstr. 15, 52074 Aachen, Germany

[7]Lead contact

*Correspondence: ec.schulz@uke.de

https://doi.org/10.1016/j.xcrp.2024.101987

minimizing collection time and sample consumption. Importantly, fixed-target data collection is not dependent on the fluidic behavior of a crystal-containing media for successful data collection, thereby dramatically improving the method's reliability over LCP extruders or liquid jets. Moreover, as the crystals are ideally stuck in their respective wells, it is the only serial crystallography sample delivery method where crystals can be systematically revisited, which has been used to track radiation damage[6,7] and for time-resolved measurements.[15] Further advantages of the fixed-target delivery platform include its convenient extension by additional hardware for, e.g., reaction initiation and environmental control, respectively.[8,16] The simplest fixed-target setups are adaptations to standard single-crystal mounts so that large crystals can be rastered across the beam[17] using existing sample preparation, on-beam visualization, and goniometers as for standard single-crystal collection. This data collection scheme leveraged computational developments from serial crystallography to produce low-dose maps of radiation-sensitive protein systems.[18] Fixed-target setups for multi-crystal measurements are designed to either sandwich (sheet-on-sheet)[19] the crystals between X-ray transparent materials or mount crystals on rigid supports with pre-made apertures.[20–23] These have been built onto pin mounts or, to accommodate larger chips with increased capacity, mounted onto x,y translation stages with longer travel ranges.[23–26] Materials are required to be X-ray transparent, particularly when shooting through the support to prevent beam attenuation and scattering artifacts, which might damage the detector. Therefore, thin polymers such as polyimide (Kapton), nylon[27,28] or mylar,[19] cyclic olefin copolymer (COC),[29] and commonly silicon[26,30] are used as support materials for chips. Silicon chips are manufactured from single crystals, so there is little to no diffuse scattering from the material. Previous work has iteratively developed a silicon chip design with 20,736 pyramid-shaped features with an 82×82 μm base tapering down to a 10×10 μm aperture.[22,23,26,30] The funneling allows microcrystal slurry to be pipetted directly onto the chip and drawn into the well by applying a gentle suctioning force. This process pre-positions crystals while removing the mother liquor, which is done with minimal suction force to prevent damaging the crystals. Due to the chips' rigidity, once aligned with the X-ray beam position, the position of each aperture can be easily calculated, thereby simplifying the motion controls required to move between each well.[24] The silicon chips are manufactured by chemically etching a Si wafer, which produces wells with the micron accuracy required. We have previously reported a chip design optimized for implementing a hit-and-return (HARE) data collection strategy for efficient time-resolved crystallography over ms-s time delays, which covers the majority of enzymatic reactions.[15,26,31] Despite these advantages, using silicon as a support material unfortunately has several drawbacks. Since silicon is brittle, damage during sample loading and chip mounting is a common nuisance. This damage varies from breaking the chips in half, rendering them completely unusable, to creating holes while pipetting the sample onto the chip, which reduces the suction force applied during loading, making the chip less effective. As a single crystal, the silicon can diffract if the beam grazes the tapered features, producing strong diffraction spots that have to be dealt with during data processing. With extended use, silicon chips often acquire an acid-resistant deposit (potentially silicon oxide), which leads to increased opacity for the infrared sample viewing system and can thereby limit their reusability. Finally, silicon-based chips are expensive (approx. 100 €) due to the materials and manufacturing techniques involved. To address these issues, we looked for a cheap and readily available material that was less brittle but also chemically inert into which the HARE chip features could be manufactured. Kapton is a cost-effective, readily available material typically utilized at X-ray sources for its low X-ray absorbance.

Here, we present a Kapton-based chip into which the HARE-chip features have been ablated using UV-laser radiation. We systematically compare two sample supports made from 50- to 125-µm-thick Kapton foils with a silicon HARE chip using five different crystallographic model systems: lysozyme, thaumatin, proteinase K, the extended spectrum β-lactamase CTX-M-14, and tryptophan synthase. Our results show that Kapton sample supports provide comparable dataset quality to silicon chips and that a sufficient number and quality of diffraction patterns can be collected from a single Kapton chip to generate a serial dataset. Kapton chips produced ca. 80% as many diffraction patterns as silicon chips and showed no difference in resolution as determined by merging statistics ($CC_{1/2}$, signal-to-noise ratio [SNR], and R_{split}) and visual inspection of $2F_{obs} - F_{calc}$ maps. The protein structures could be refined with R_{free}/R_{work} that showed no difference between chip materials. Finally, a comparison of the background scattering from other X-ray transparent polymers shows the viability to use other X-ray transparent polymers.

RESULTS

Chip manufacture and quality control

High-quality laser ablation in dielectrics such as Kapton requires a highly localized energy input. This can be attained through a substantial amount of linear absorption. In Kapton, this requires an input photon energy <3 eV, corresponding to the UV range. Ultrashort pulses (USPs), which are below the electron-phonon relaxation time (<10 ps), maximize the proportion of absorbed energy used for material ablation rather than heating. Therefore, optimal ablation in Kapton occurs using ultrashort UV pulses (UV-USPs). For a typical USP laser medium such as Yb:YAG with a fundamental wavelength of 1,030 nm, frequency conversion to at least the third harmonic is required. In order to perform flexible and precise surface ablation of a dense microhole pattern <10 µm such as the HARE chip, a fast galvo scanner deflects the beam through a microscope objective instead of a commonly used F-theta lens (Figure S1).[32] For this setup, different UV-laser-compatible microscope objectives with varying magnifications can currently yield focal diameters ranging from 6.2 µm down to 0.5 µm. For manufacturing the HARE chip, a 6.2 µm spot size was selected for higher throughput and a larger scan field. The whole chip is 25 × 25 mm² in size; therefore, multiple scan fields were stitched together via linear xy axes movements for the large machining area. The Kapton was mounted into a specialized holder positioning the sheet between metal frames that, when screwed together, pulled the Kapton over a raised rim, providing tension and flattening the processing surface (Figure 1A). The pyramid-shaped features were formed by ablating consecutively smaller squares into the well center in a cross-hatching pattern (Figure 1B). After ablation, a residual film thickness of 8 µm remained. The well aperture was formed by percussion laser drilling, a sequence of laser pulses causing repeated indentations in the material, eventually creating a round exit hole. UV-USP laser ablation fidelity was assessed by light microscopy and 3D reconstructions from confocal microscopy of the Kapton chip. Magnified images (Figure 1C) clearly show the anticipated HARE chip 6 × 6 compartment tessellation and that each compartment comprises 24 × 24 evenly spaced features. Confocal microscopy of the 50 µm Kapton chip was used to assess whether the features met the geometrical dimensions expected. Height profiles from 20 features were extracted and fitted (Figure S2) to measure the feature width and separation between features. The average feature width was 80.4 ± 0.8 µm, while the average distance between the center of adjacent features was 150.6 ± 0.4 µm. This agrees well with the HARE chip design of an 82 µm feature width and a 150 µm separation between feature centers. Light microscopy of single wells (Figure 1C) estimated the feature aperture
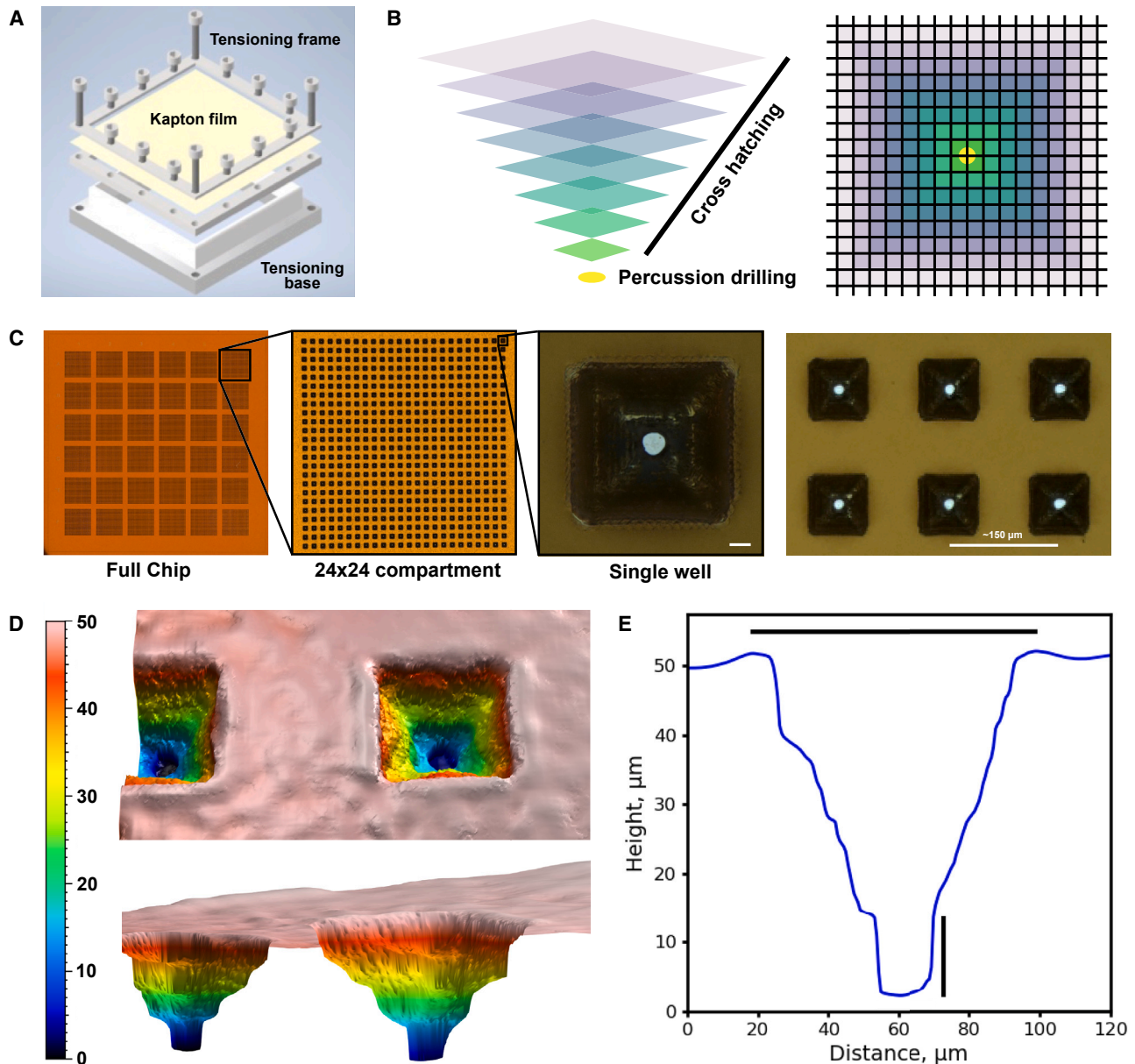
Figure 1. Kapton HARE-chip manufacture via laser ablation

(A) CAD exploded view of the tensioning frame CAD design.

(B) Feature processing strategy and cross-hatching pattern that forms the pyramidal wells.

(C) Light microscopy images for the overall Kapton chip, a 24 × 24 compartment, a single feature (scale bar: 10 μm), and side-by-side wells.

(D) A 3D reconstructed representation of the ablated features from confocal microscopy viewed from above looking into the feature and a side-on cross-section. The scale bar is given in μm.

(E) Profile extracted from the confocal microscopy image representing a central slice through the feature. Scale bars: 80.1 μm (horizontal bar; well width) and 14.1 μm (vertical bar).

at 12 μm, while the confocal profile (Figure 1E) through the feature center gives a 14.5 μm diameter, both slightly larger than the 10 μm for the silicon chips. Finally, the profiles reveal that the percussion drilling went through the last 10–14 μm (Figure 1E) to form the feature's exit aperture. Therefore, the UV-USP laser process has the high spatial accuracy and reproducibility required to produce HARE chip features within Kapton within a few microns from the design specifications (Figure S2).

Table 1. Hit rate comparison

Protein	Crystal volume (µm³)	Crystal concentration, crystal/mL (×10⁷)	Silicon		50 µm Kapton			100 µm Kapton		
			Average hits	Chip-to-chip variance (± %)	Average hits	Chip-to-chip variance (± %)	Difference from silicon (%)	Average hits	Chip-to-chip variance (± %)	Difference from silicon (%)
Tryptophan synthase	1,920	1.56	3,362	48.37	3,324	17.67	−1.14	1,957	11.55	−41.78
Thaumatin	2,500	2.01	5,165	37.00	5,755	21.35	11.44	2,408	35.96	−53.38
CTXM-14	3,375	0.78	9,247	13.83	7,619	0.88	−17.61	5,352	10.63	−42.12
Lysozyme	85,184	0.65	14,470	34.35	8,031	36.42	−44.50	10,734	19.64	−25.82
Proteinase K	1,000,000	0.16	15,807	14.72	9,340	21.86	−40.91	14,528	16.09	−8.09
Average	–	–	–	29.65	–	19.63	−18.54	–	18.77	−34.24

Hit rate statistics listing, crystal volume and concentration, the average number of hits, the chip-to-chip variance, and the difference of the Kapton chips from the silicon chips.

Serial crystallography

Serial measurements were performed at the EMBL P14-2 (T-REXX) endstation at the PETRA-III synchrotron (DESY, Hamburg, Germany). The different samples were loaded with protein crystals in a humidified environment to prevent dehydration as described previously.[16] Both silicon and Kapton chips were loaded with ∼ 80 − 120 µL of the sample, which is sufficient to cover the chip with crystal suspension, and excess mother liquor was removed. The Kapton chips were then mounted into the standard sample holder and were then aligned and rastered in the same way,[26] thus being obviously compatible with setups that can utilize the silicon HARE chip as described previously.[24] Initially, however, the Kapton chips did present challenges for alignment. For general chip alignment, the apertures from the same wells in the bottom right, bottom left, and top left compartments are aligned at the beam focal point, and their position is recorded. The required positions for all other wells across the chip are then calculated on that basis. As a quality control, the chip is moved to an arbitrary well, and visual inspection ensures it is at the aperture center, which confirms proper chip alignment.

Systematic comparison of crystal hit rates and distribution

For a direct comparison between Kapton and silicon chips, microcrystalline slurries of five model proteins were prepared: thaumatin, lysozyme, proteinase K, CTX-M-14, and tryptophan synthase. To assess the sample loading variability, three chips of each material were measured for each protein sample. Prior to loading, all chips were subjected to a selective-wetting procedure that is glow discharged to minimize the effect of water tension while removing the mother liquor, helping to disperse the crystals evenly across the chip. Proteinase K, lysozyme, and CTX-M-14 had sufficient crystal density (Table 1) to produce enough diffraction patterns for a serial dataset from a single chip. Merging the three repeats for each sample yielded a 1.7-Å-resolution dataset for all proteins except tryptophan synthase, which diffracted to 2.0–2.1 Å (Tables 2, 3, 4, 5, and 6). Surprisingly, the variation of diffraction patterns per chip for a given protein and chip material was higher for the silicon (30%) than for the Kapton (19%) chips. We speculate that this could be related to the distribution of the suction during chip loading. The Kapton chips provide a tighter seal on the chip-loading device, which could explain the reduced chip-to-chip variance. More importantly, while several identical silicon chips were used throughout the experiment, only a single Kapton chip of each thickness was available. Comparing the average number of hits between chips, Kapton consistently produced less hits when compared to silicon. The decrease was consistent across samples despite differing crystal concentration, morphology, and handling users (Figure 2). While the 125 µm Kapton chip showed a 34% reduction, the 50 µm Kapton

Table 2. Data collection and refinement statistics for thaumatin

Dataset	Thaumatin, silicon	Thaumatin, 50 µm Kapton	Thaumatin, 125 µm Kapton
Data collection			
Collection temperature (K)	293	293	293
Space group	$P4_12_12$	$P4_12_12$	$P4_12_12$
No. of diffraction images	16,466	18,855	8,192
No. of indexed lattices	20,325	23,139	9,115
Indexing rate (%)	123.4	122.7	111.3
No. of total reflections	5,045,991	5,340,953	2,303,870
No. of unique reflections	33,366	29,560	33,424
Unit cell parameters			
a,b,c (Å)	58.20,58.20,150.90	58.20,58.20,150.90	58.20,58.20,150.90
α,β,γ (°)	90,90,90	90,90,90	90,90,90
Data parameters			
Resolution (Å)	54.30–1.7 (1.76–1.7)	54.30–1.7 (1.76–1.7)	54.30–1.7 (1.76–1.7)
R_{split} (%)	15.68 (84.00)	12.3 (94.2)	23.3 (180.5)
SNR ($I/\sigma(I)$)	5.23 (0.84)	5.93 (1.11)	3.30 (0.59)
$CC_{1/2}$	0.962 (0.519)	0.982 (0.497)	0.935 (0.203)
CC*	0.992 (0.827)	0.996 (0.815)	0.983 (0.582)
Completeness (%)	100 (100)	100 (100)	100 (100)
Multiplicity	151.2	180.7	73.4
Refinement			
Resolution range for refinement (Å)	54.30–1.7 (1.76–1.7)	54.30–1.7 (1.76–1.7)	54.30–1.7 (1.76–1.7)
Reflections in refinement	29,456 (2,898)	29,449 (2,893)	29,431 (2,882)
R_{work} (%)	16.47	16.25	18.44
R_{free} (%)	18.36	18.36	21.38
Average B-factor	23.34	24.92	26.04
No. of atoms	1,762	1,709	1,789
Protein	1,583	1,572	1,600
Ligands/ions	10	10	10
Water	169	127	179
RMS deviations			
Bond lengths (Å)	0.006	0.006	0.012
Bond angles (°)	0.85	0.87	1.20
Ramachandran outliers (%)			
Favored	98.54	98.04	97.56
Allowed	1.46	1.96	2.44
Outliers	0.00	0.00	0.00

Values in the highest resolution shell are shown in parentheses. Data for each chip material are merged from three independent data collections.

chip showed only a 19% reduction (Table 1). For the 50 µm chip, this was within the chip-to-chip variation, with only the thaumatin sample producing more hits from the 50 µm Kapton chip then from silicon. Overall, there is a direct positive correlation between hit rate and crystal size; that is, larger crystals that are more easily trapped within the features of a chip also display higher hit rates (Figure 2). This increase is not uniform between Kapton thickness, with the hit rate increasing more for larger crystals with 125 µm Kapton compared to 50 µm. Since the thicker Kapton provides deeper features, it is likely that the wells accommodate larger crystals more easily. To illustrate loading reproducibility specific to the chip material, color-coded combined hit maps were calculated for all samples. Each color represents how many chips in which a given feature produced at least one indexed diffraction pattern (Figure 2). Effective chip loading should evenly disperse the sample across the chip to utilize as many features as possible. The combined hit maps showed that for all chip materials, every sample had crystals distributed across the entire chip surface. Thaumatin and tryptophan synthase produced combined hit maps where most

Table 3. Data collection and refinement statistics for lysozyme

Dataset	Lysozyme, silicon	Lysozyme, 50 μm Kapton	Lysozyme, 125 μm Kapton
Data collection			
Collection temperature (K)	293	293	293
Space group	$P4_32_12$	$P4_32_12$	$P4_32_12$
No. of diffraction images	43,411	24,092	32,201
No. of indexed lattices	92,338	41,603	53,969
Indexing rate (%)	212.7	172.7	167.6
No. of total reflections	18,233,733	8,963,463	10,299,080
No. of unique reflections	15,691	15,684	15,658
Unit cell parameters			
a,b,c (Å)	79.00,79.00,38.00	79.00,79.00,38.00	79.00,79.00,38.00
α,β,γ (°)	90,90,90	90,90,90	90,90,90
Data parameters			
Resolution (Å)	55.86–1.7 (1.761–1.7)	55.86–1.7 (1.761–1.7)	55.86–1.7 (1.761–1.7)
R_{split} (%)	8.26 (10.4)	8.28 (11.7)	8.83 (11.02)
SNR ($I/\sigma(I)$)	13.07 (10.95)	12.54 (8.68)	12.02 (8.84)
$CC_{1/2}$	0.983 (0.973)	0.988 (0.975)	0.986 (0.975)
CC*	0.997 (0.993)	0.997 (0.993)	0.996 (0.994)
Completeness (%)	99.95 (100)	99.99 (100)	95.16 (100)
Multiplicity	1,162.1	571.5	657.8
Refinement			
Resolution range for refinement (Å)	55.86–1.7 (1.761–1.7)	55.86–1.7 (1.761–1.7)	55.86–1.7 (1.761–1.7)
Reflections in refinement	13,750 (1,344)	13,755 (1,344)	13,754 (1,342)
R_{work} (%)	18.60	16.10	16.81
R_{free} (%)	18.81	16.67	17.53
Average B-factor	17.69	19.24	19.43
No. of atoms	1,126	1,126	1,126
Protein	1,054	1,054	1,054
Ligands/ions	7	7	7
Water	65	65	65
RMS deviations			
Bond lengths (Å)	0.007	0.007	0.007
Bond angles (°)	0.89	0.89	0.92
Ramachandran outliers (%)			
Favored	99.21	98.43	98.43
Allowed	0.79	1.57	1.57
Outliers	0.00	0.00	0.00

Values in the highest resolution shell are shown in parentheses. Data for each chip material are merged from three independent data-collections.

features were visited once across the three chips (Figure 2). CTX-M-14, lysozyme, and proteinase K had higher hit rates and therefore more features and were visited repeatedly across the three chips. In general, however, the different chip materials show the same distribution of crystals.

Electron density comparison

Convincing electron density could be retrieved for data from Kapton chips with good R_{free}/R_{work} values (Figure S3) across all model proteins. Lysozyme was refined for each chip type to an R_{free} of less than 20%. The 50 μm Kapton and 125 μm Kapton have comparable R_{free} values at 16.6% and 17.5%, respectively, while the silicon data refined to an R_{free} at 18.8% (Table 3; Figure S3). The Kapton chips generally produce similar R-factors to the silicon chips, and data statistics do not appear to be compromised by the chip material. However, for the 125 μm Kapton chips, slightly higher R-factors (1%–2%) as well as lower SNRs can be observed for CTX-M-14, thaumatin,

Table 4. Data collection and refinement statistics for proteinase K

Dataset	Proteinase K, silicon	Proteinase K, 50 μm Kapton	Proteinase K, 125 μm Kapton
Data collection			
Collection temperature (K)	293	293	293
Space group	$P4_32_12$	$P4_32_12$	$P4_32_12$
No. of diffraction images	47,223	28,021	43,584
No. of indexed lattices	128,326	69,080	123,592
Indexing rate (%)	271.7	246.5	283.6
No. of total reflections	32,996	32,794	32,848
No. of unique reflections	41,713,434	29,165,666	38,818,608
Unit cell parameters			
a,b,c (Å)	68.50,68.50,108.75	68.50,68.50,108.75	68.50,68.50,108.75
α,β,γ (°)	90,90,90	90,90,90	90,90,90
Data parameters			
Resolution (Å)	57.96–1.66 (1.73–1.66)	57.96–1.66 (1.73–1.66)	57.96–1.66 (1.73–1.66)
R_{split} (%)	6.86 (8.43)	6.69 (9.46)	5.91 (7.27)
SNR (I/σ(I))	17.14 (13.12)	17.29 (11.34)	19.23 (14.68)
$CC_{1/2}$	0.991 (0.981)	0.991 (0.978)	0.993 (0.987)
CC*	0.998 (0.995)	0.998 (0.994)	0.998 (0.997)
Completeness (%)	100 (100)	100 (100)	100 (100)
Multiplicity	1,264.2	889.4	1,181.8
Refinement			
Resolution range for refinement (Å)	57.96–1.66 (1.73–1.66)	57.96–1.66 (1.68–1.63)	57.96–1.66 (1.71–1.66)
Reflections in refinement	31,322	32,652	31,323
R_{work} (%)	14.97	13.78	14.44
R_{free} (%)	17.83	16.21	17.85
Average B-factor	12.62	12.37	12.66
No. of atoms	2,263	2,332	2,321
Protein	2,136	2,190	2,205
Ligands/ions	5	5	5
Water	122	137	111
RMS deviations			
Bond lengths (Å)	0.006	0.012	0.016
Bond angles (°)	0.80	1.21	1.32
Ramachandran outliers (%)			
Favored	96.75	96.75	96.75
Allowed	3.25	3.25	3.25
Outliers	0.00	0.00	0.00

Values in the highest resolution shell are shown in parentheses. Data for each chip material are merged from three independent data collections.

and tryptophane synthase, which are the samples with the smallest crystal size. We speculate that this could be related to a higher amount of residual mother liquor that could be retained within the features of the 125 μm Kapton chips, which thereby could have an effect on diffraction quality parameters.

Kapton HARE chips can yield equivalent data quality

For each protein sample and chip type, data from all three chips were merged. Irrespective of the chip material, most protein samples provided a sufficient number of diffraction patterns for a robust dataset with diffraction to the detector edge (1.7 Å). To assess data quality, plots for merging and refinement statistics for both Kapton and silicon datasets for all proteins were generated as previously reported[7] and show no significant difference between the two materials (Figure 3). Despite the diffraction rings visible in radial averages for Kapton, the merged SNR and R_{free} profiles were essentially identical (Figure 3). This agrees with the minimal difference in the overall background between the two materials (Figure 4B). We note that for

Table 5. Data collection and refinement statistics for CTX-M-14

Dataset	CTX-M-14, silicon	CTX-M-14, 50 μm Kapton	CTX-M-14, 125 μm Kapton
Data collection			
Collection temperature (K)	293	293	293
Space group	$P3_221$	$P3_221$	$P3_221$
No. of diffraction images	27,740	22,856	16,056
No. of indexed lattices	39,483	33,323	21,161
Indexing rate (%)	142.3	145.8	131.8
No. of total reflections	31,752	31,722	31,785
No. of unique reflections	13,417,681	10,659,697	6,724,670
Unit cell parameters			
a,b,c (Å)	42.15,42.15,234.20	42.15,42.15,234.20	42.15,42.15,234.20
α,β,γ (°)	90,90,120	90,90,120	90,90,120
Data parameters			
Resolution (Å)	78.07–1.62 (1.68–1.62)	78.07–1.63 (1.68–1.63)	78.07–1.63 (1.68–1.63)
R_{split} (%)	11.32 (413.08)	9.79 (72.7)	13.68 (107.96)
SNR ($I/\sigma(I)$)	7.48 (1.31)	7.52 (1.40)	5.34 (0.95)
$CC_{1/2}$	0.993 (0.019)	0.983 (0.686)	0.971 (0.551)
CC*	0.993 (0.019)	0.996 (0.902)	0.993 (0.843)
Completeness (%)	95.05 (87.27)	99.99 (99.93)	100 (100)
Multiplicity	422.6	336.0	211.6
Refinement			
Resolution range for refinement (Å)	78.07–1.63 (1.68–1.63)	78.07–1.63 (1.68–1.63)	78.07–1.63 (1.68–1.63)
Reflections in refinement	31,196	31,412	31,435
R_{work} (%)	15.53	15.55	16.48
R_{free} (%)	18.80	18.25	19.54
Average B-factor	29.90	29.41	30.89
No. of atoms	2,244	2,261	2,251
Protein	2,074	2,091	2,082
Ligands/ions	5	5	5
Water	165	165	164
RMS deviations			
Bond lengths (Å)	0.01	0.01	0.005
Bond angles (°)	1.04	1.08	0.78
Ramachandran outliers (%)			
Favored	98.45	98.06	98.45
Allowed	1.16	1.55	1.16
Outliers	0.39	0.39	0.39

Values in the highest resolution shell are shown in parentheses. Data for each chip material are merged from three independent data collections.

proteinase K, the Kapton datasets show improved statistics compared to silicon, but as this effect is not observed in the other samples, it is unlikely to represent an intrinsic feature of the Kapton chips. As outlined above, it is possible that greater residual mother liquor reduced the data quality on a per-image basis, as the R_{split} and $CC_{1/2}$ start to converge as more data are merged. Finally, the similar R_{free} profiles in relation to resolution between chip materials show the equivalent quality and usability of both support materials.

The Kapton chips do not induce orientational preference

A unique caveat for fixed targets is that loading crystals onto a support may induce a preferred orientation and prevent measuring some reflections. We have plotted histograms for the distributions of angles needed to orientate the reciprocal axis onto the real space axis for each sample. The distributions for all the support materials used in this study are plotted together for each sample and axis comparison (Figure S4). In all cases, the crystals are sampled across enough orientations for sufficient

Table 6. Data collection and refinement statistics for tryptophan synthase

| Dataset	Tryptophan synthase, silicon	Tryptophan synthase, 50 μm Kapton	Tryptophan synthase, 125 μm Kapton
Data collection			
Collection temperature (K)	293	293	293
Space group	C2	C2	C2
No. of diffraction images	11,711	9,965	5,572
No. of indexed lattices	13,060	10,965	6,445
Indexing rate (%)	111.5	110.0	115.7
No. of total reflections	2,539,995	2,216,059	1,223,454
No. of unique reflections	51,012	51,011	51,011
Unit cell parameters			
a,b,c (Å)	183.60,61.50,67.60	183.60,61.50,67.60	183.60,61.50,67.60
α,β,γ (°)	90,94.55,90	90,94.55,90	90,94.55,90
Data parameters			
Resolution (Å)	91.5–2.0 (2.072–2.00)	91.5–2.11 (2.185–2.11)	91.5–2.2 (2.279–2.2)
R_{split} (%)	23.76 (107.46)	23.02 (95.11)	30.68 (103.86)
SNR ($I/\sigma(I)$)	3.25 (1.01)	3.33 (1.15)	2.74 (1.09)
$CC_{1/2}$	0.943 (0.505)	0.953 (0.533)	0.898 (0.424)
CC*	0.985 (0.819)	0.988 (0.834)	0.973 (0.772)
Completeness (%)	100 (100)	100 (100)	100 (99.97)
Multiplicity	49.8	43.4	24.0
Refinement			
Resolution range for refinement (Å)	91.5–2.0 (2.072–2.00)	91.5–2.11 (2.185–2.11)	91.5–2.2 (2.279–2.2)
Reflections in refinement	41,902 (1923)	43,481 (4324)	41,902 (1924)
R_{work} (%)	18.02	19.10	18.02
R_{free} (%)	22.17	21.09	22.17
Average B-factor	38.70	38.60	38.70
No. of atoms	5,133	5,153	5,133
Protein	4,946	4,949	4,946
Ligands/ions	17	17	17
Water	170	187	170
RMS deviations			
Bond lengths (Å)	0.007	0.007	0.007
Bond angles (°)	0.91	0.87	0.91
Ramachandran outliers (%)			
Favored	98.29	98.29	98.29
Allowed	1.71	1.55	1.71
Outliers	0.00	0.16	0.00

Values in the highest resolution shell are shown in parentheses. Data for each chip material are merged from three independent data collections.

redundancy in all reflections. For several panels, there are distinct peaks around certain axes, and these are probably a product of the symmetry of the crystals themselves; for example, proteinase K and lysozyme share a $P4_32_12$ space group and show broadly similar distributions. Importantly, there is no clear orientation preference induced by the use of Kapton chips compared to the silicon chips. Some shifts in the distributions between materials are observed for certain reciprocal and real-space lattice comparisons, for example a* distribution around the z axis in proteinase K. Here, the distribution shift is better explained by the thickness of the chip with 125 μm Kapton and the silicon (100 μm) chips producing a bimodal distribution compared to the Kapton 50 μm, which produces a more uniform distribution.

Comparison of background scattering between chip materials

The silicon chips are manufactured from a single crystal, which minimizes general scattering from the support material but produces strong reflections at specific
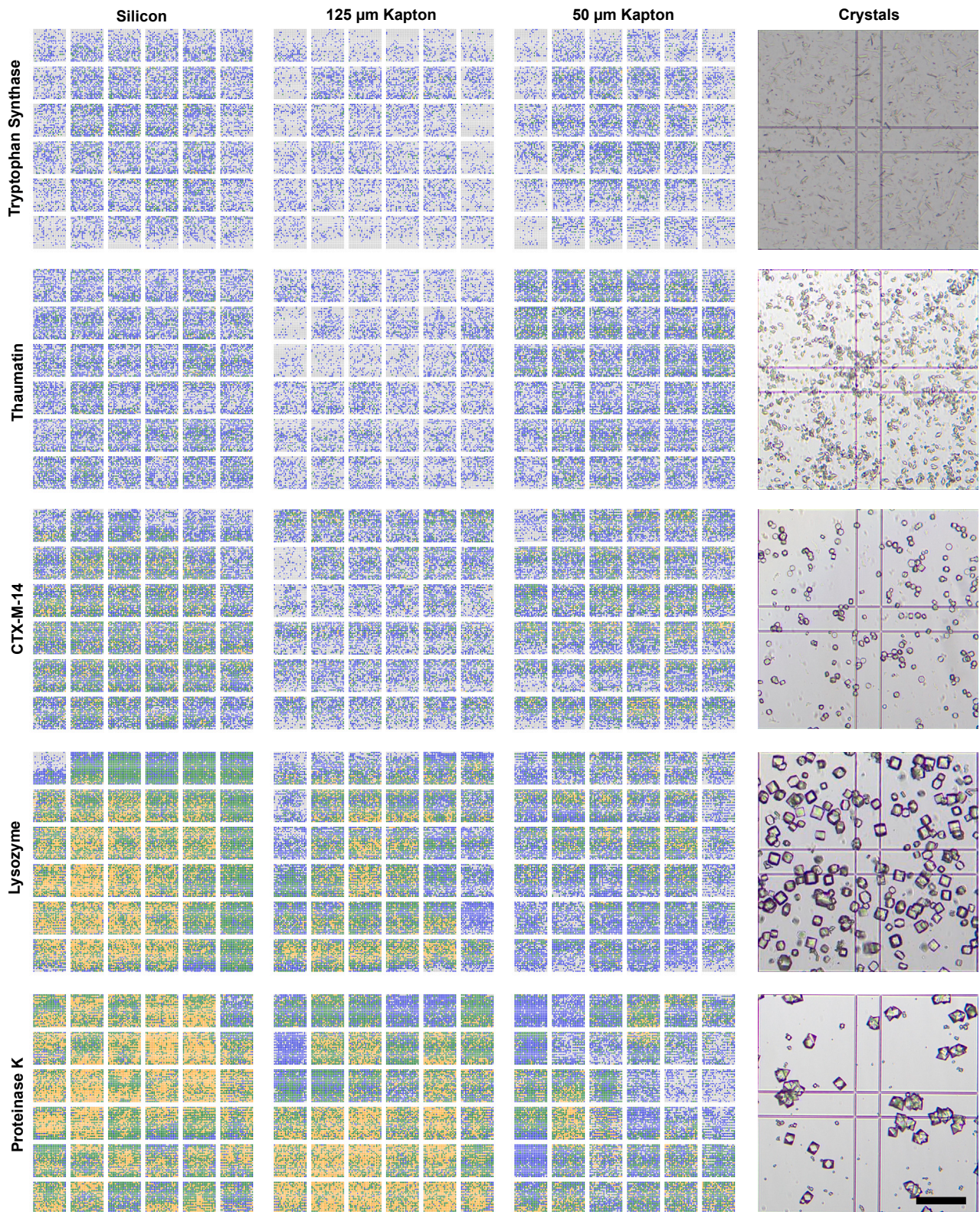
**Figure 2. Chip loading comparison**
To illustrate loading patterns, combined hit maps were generated: each image represents the superposition of the hit maps from three chips for the respective protein and material. Each spot corresponds to a feature on the chip. Color code: gray, no hit; blue, diffraction in 1/3 chips; green, diffraction in 2/3 chips; and yellow, diffraction in 3/3 chips. A magnified image for each of the protein samples is shown. Scale bar: 100 μm. The length of each square in the cell-counting chamber is 200 μm.

detector positions (Figure 4A). Kapton, as an amorphous polymer, scatters X-ray photons more uniformly across the detector. To assess the background scattering, approximately 2,000 images for each chip material were radially averaged (Figure 4). To assess material-specific differences in chip alignment accuracy, we compared a well-aligned image with a misaligned image. For well-aligned chips, the overall radial profiles of Kapton and silicon are highly similar (Figure 4B). This suggests that there is little difference between Kapton and silicon background scattering and, therefore, that the primary background contribution for all chip materials originates from air scatter. This agrees with similar merged signal-to-noise profiles between the chip materials (Figure 3). Upon misalignment, however, silicon produces a peak at high resolution (1.63 Å). Unsurprisingly, the misaligned 125 μm Kapton produces slightly increased scattering across the radial profile compared to the 50 μm Kapton. The 125 μm Kapton shows an approximately 100% increase in characteristic peaks (2–5 Å), which are unique to Kapton. A noticeable feature in the 125 μm Kapton is a strong low-resolution spike (at ca. 20 Å) from the 125 μm Kapton, which is persistent for aligned or unaligned images and more prevalent in misaligned chips. Irrespective of the Kapton thicknesses, weak ring features are visible between 3 and 10 Å, possibly arising from partial crystallinity in the Kapton giving rise to weak powder diffraction rings.

### Other potential polymers for serial crystallography supports
While Kapton supports are a convenient material for the laser ablation process, there are several other amorphous polymers with low X-ray absorbance that are routinely used at synchrotrons. To test whether these could serve as a support material, we measured the scattering profiles for COC at 125 and 12 μm thickness, as well as 2.5 μm mylar and a corner from both Kapton foils at the EMBL beamline P13 (DESY) (Figure S5A). As a reference, we recorded the background profile, which shows a uniform drop-off with increasing theta, leaving minimal background scattering at high resolution (Figure S5A). Upon X-ray exposure, the different polymers display scattering across the detector, with distinct scattering peaks after background subtraction (Figure S5B). Mylar showed the least additional scattering but was also too thin (2.5 μm) for meaningful chip production. As is also visible from the diffraction images, Kapton leads to distinct ring scattering, visible in the scattering profile as features between 3 and 10 Å. The intensity of these scattering features scales with Kapton thickness (Figure S5B). Interestingly, the thicker Kapton produces a strong feature at low resolution not seen in the thinner material. This agrees with the Kapton scattering seen during data collection with the chips, as similar ring features were observed at this resolution. However, during data collection, these features were less pronounced. We anticipate that this reduction is due to (1) contributions from residual mother liquor and protein crystals and (2) shooting through the well aperture providing less material to scatter from. In contrast to Kapton or mylar, COC produces a single strong peak around 5 Å and negligible background scattering at higher resolutions. These properties make COC a promising fixed-target support material for serial crystallography. Indeed, COC was recently used by Carillo et al. to manufacture serial crystallography chips, which also show a similar scattering peak without affecting data quality.[29]
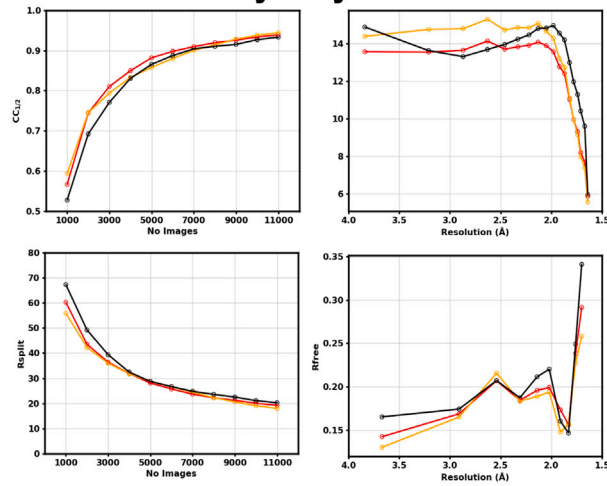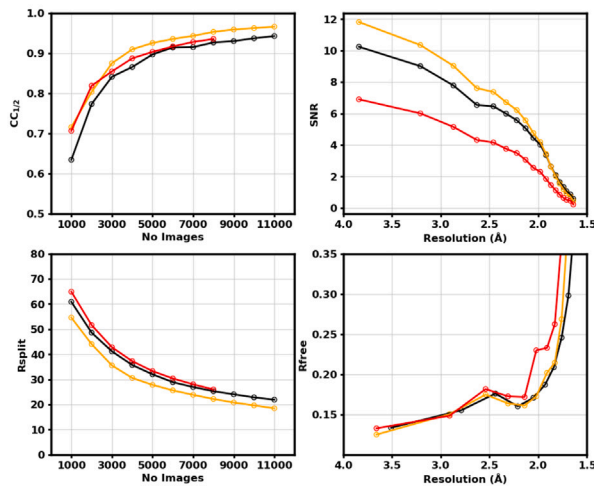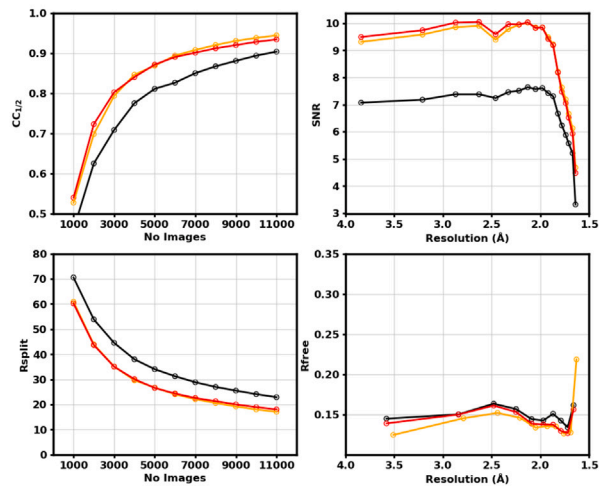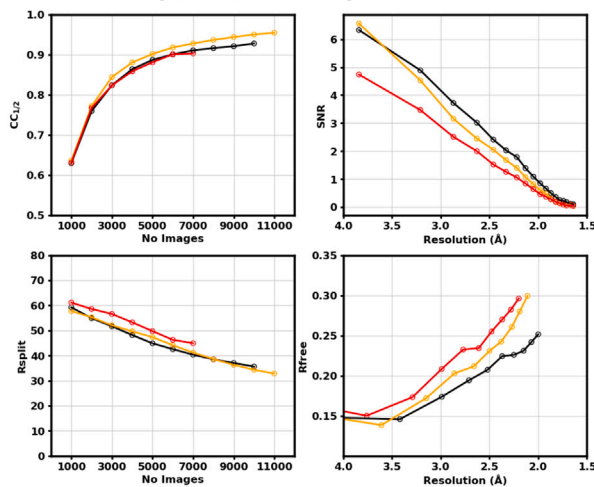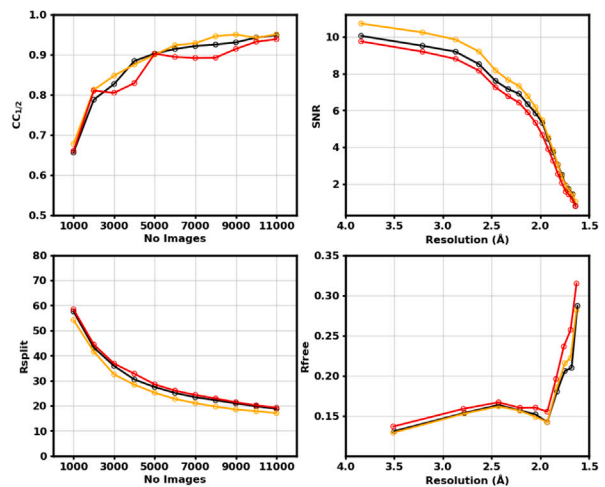
**Figure 3. Data quality comparison**

Data quality comparison for thaumatin, proteinase K, CTX-M-14, and tryptophan synthase. Serial merging and refinement statistics are compared, with silicon chip (black), 50 μm Kapton (orange), and 125 μm Kapton (red). R_{split} and CC1/2 are plotted while merging an increasing number of crystals. The SNR is the output from a 22,000 crystal dataset except for where there are fewer than 22,000 crystals, in which case it comprises all data. Separately, the R_{free} is reported from refinement against all crystals indexed for the given material.

DISCUSSION

Serial crystallography is distinctively useful for time-resolved applications, a growing methodology to correlate protein structure and dynamics.[2,5,7,11,33] Our previous work developed the HARE chip, optimized for efficient time-resolved experiments. Design considerations included optimizing compartment size to maximize feature areas for increased crystal throughput while minimizing chip fragility. Moreover, the pyramidal shape of the features prevents orientational bias of the crystals, and their regular spacing not only allows optical excitation without light contamination but also optimizes the HARE algorithm, where features are revisited in a time-efficient manner, enabling time delays in the ms-s time domain.[15,26] In addition, the HARE chips support efficient mother liquor removal, enabling ligand addition by the liquid application method for time-resolved analyses method.[16] The HARE design has been proven highly beneficial in addressing biologically relevant timescales due to both the versatile means of reaction initiation and compatibility with variable crystal sizes, combined with frugal sample consumption.[11,26]

Therefore, we argue that this design has the potential to serve as a standard for a future TR-SSX fixed targets. In this light, we aimed at assessing whether X-ray transparent polymers following the HARE design are a practically useful and economically competitive alternative to silicon-based chips. A variety of fixed-target solutions have previously utilized X-ray transparent polymers, where crystals were sandwiched between Kapton, mylar, COC layers, or a nylon mesh.[19,27,34–36] These are straightforward and cost-effective strategies but compromise on data quality, as the mother liquor cannot be removed, and have limited or no crystal positioning. Unfortunately, they also forgo the ability to add ligands by *in situ* mixing approaches, the most convenient way of reaction initiation. Kapton has been used either as a grid support material for single (micro)crystals or as small meshes on SPINE mounts.[37] These have a similar footprint to previous silicon chips fitted onto rotation mounts[20,21] but are cheaper and can be rotated in the beam without risking generating intense Bragg reflections from the substrate material. By contrast, our Kapton chips follow the same dimensions and optimized design parameters as the full-sized silicon HARE chips, enabling a direct and systematic comparison between silicon and Kapton as support materials.

Via laser ablation, we obtained micron-sized, pyramid-shaped features in Kapton. Small differences are observed between the HARE chip design and the Kapton prototypes; the well widths, for example, are 2 μm smaller than their silicon counterparts. Due to the manufacturing strategy, the features in the Kapton chips do not extend completely through the material, causing smaller feature volumes. The hole at the bottom is generated during the last step via percussion drilling. We speculated whether this explained the reduced indexing rate for Kapton chips, but the reduction is not consistent with Kapton thickness. Another difference is the Kapton flexibility, which requires some changes in the experimental workflow. Alignment procedures proved to be more challenging with the Kapton chips due to more demanding visualization and positioning of the feature centers. A convenient workaround lies in simply taping the Kapton chip to the sample holder, creating a tension across the chip to reduce flexing of the foil. This improved the hit and indexing rate, although more comprehensive testing is required. As such, it is clear that a
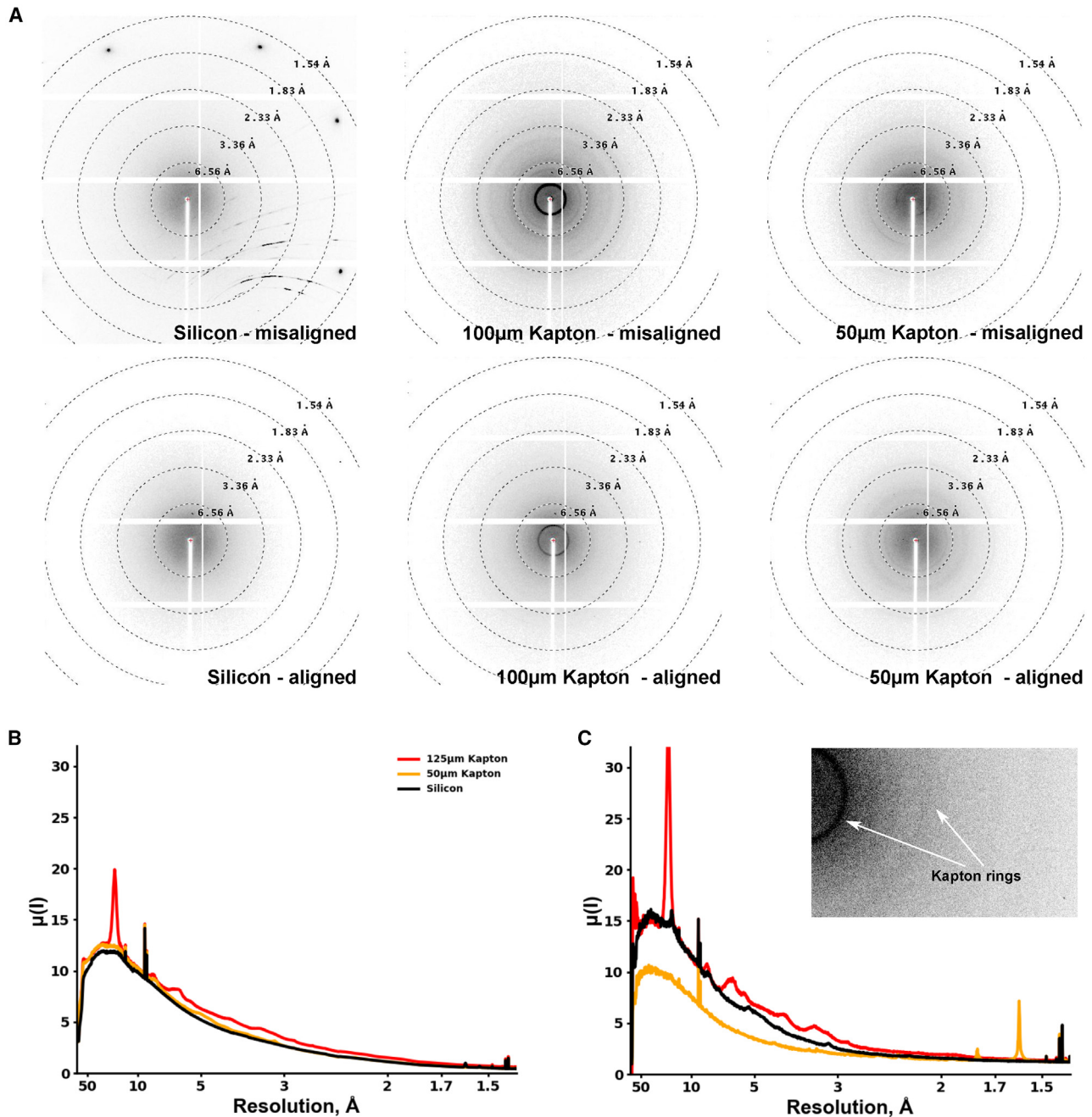
Figure 4. Background scattering comparison

Comparison between silicon and Kapton chip misalignment artifacts and background scattering: (A) individual images representing aligned and misaligned apertures for silicon and 125 μm and 50 μm Kapton. Radial profiles were calculated from approximately 2,000 averaged images per chip material, (B) reducing variability due to chip alignment. Misaligned images in (A) were also radially averaged (C). Inset shows the ring effects observed in the 125 μm Kapton data.

custom-made sample mount for Kapton chips should address both potential feature distortion and alignment issues. Nevertheless, the alignment difficulties influence neither chip loading nor the ability to hit crystals. If hit rates fell consistently scanning across the chips, then this would indicate a geometrically defined systematic drift in positioning at the well center.

Crystal size varies across the different samples; typically, smaller crystals yielded higher hit rates in the 50 μm Kapton compared to 125 μm Kapton, which reverses as the crystal sizes get larger. This is understandable for the larger crystals, which are between 40 and 50 μm, approximately the depth of the well. It is less clear why smaller crystals would not sit in the larger wells. Previous studies suggest that the larger volume of residual mother liquor maybe able to refloat the crystals out of the well[37] during loading. Alternatively, the deeper well may allow the crystals to orientate such that they could go through the well aperture, which is slightly larger in the Kapton chips. Although larger apertures do not influence the 50 μm average hits compared to silicon (Table 1), it should be noted that for the CTX-M-14 repeats, the 50 μm Kapton showed a remarkable consistency compared to the other samples. CTX-M-14 is a well-behaved sample with a highly homogeneous crystal distribution in the batch productions. We suspect that further measurements would have a higher variance. We speculate that the CTX-M-14 crystal size was optimal for the well volume in the thin Kapton chips, producing repeatable loading. However, further work on the relationship between well and crystal size is required.

Apart from practical differences, the merged datasets from Kapton HARE chips provide highly comparable data quality: only minor distributional changes in the crystal orientations can be observed, and the refined structures display equivalent $2F_o - F_c$ electron density. The crystal orientations are not significantly shifted between Kapton or silicon chips. This makes sense, as the chip and well shape are anticipated to have a greater influence on the crystal orientation than the chip material. The shifted orientations that do occur are typically between thinner and thicker chips, which will influence the well geometry. For example, in proteinase K, axis a* versus z distribution is bimodal in the thicker chips, which may have more space in the well for the crystals to rotate in the well. Finally, we note that preferred orientation as a problem is not well assessed in serial crystallography, and a more in-depth analysis is still needed on this question. The comparable data quality also suggests that the additional scattering provided by the Kapton HARE chips does not directly compromise the data. The similar scattering profiles for other chip materials indicate that these could also be valid alternatives. Mylar showed very little additional scattering; however, to enable a practically useful chip, a greater mylar thickness would be required. COC, on the other hand, showed only a single distinct diffraction ring near 5 Å resolution and contributes comparably little to the scattering at higher resolutions. Indeed, the viability of COC as a chip material has been recently demonstrated by Carillo et al. utilizing a stamping methodology, albeit not following the HARE design pattern.[29] Here, pressure and heat were applied to COC or COP through an etched template, which stamps the features into the material. However, the stamping methodology has drawbacks, e.g., variable aperture sizes across the chip. This is due to horizontal material displacement rather than its removal. This increases the thickness between features and causes a reduction in aperture size to approximately <5 μm, 15 wells from the edge. We anticipate that a chip with compartments, such as the HARE chip, would minimize this limitation in the stamping process, potentially also improving the uneven crystal distribution across these chips, which are not seen in our results. Moreover, recent light-triggered time-resolved X-ray crystallography experiments with these "MISP" chips showed considerable light contamination between wells even when deploying interleaving strategies and making the polymer material opaque.[38] In the HARE chip design, the wells are spaced slightly further apart (150 μm) with smaller well widths to limit light contamination; furthermore, the compartment sizes are 24 × 24, which permits a convenient implementation of sparse interleaving strategies to further prevent light contamination. Hence, considering its practical advantages and low X-ray

scattering background, a COC-based chip following the HARE design pattern appears to be an interesting alternative and a clear avenue for future development.

Aiming for cost-effective alternatives to silicon for serial crystallography chips, Kapton and other polymers are economically highly competitive materials. For the production of the Kapton-HARE chip prototypes, we used a single-beam laser setup, with a chip production time of approximately 10 h. Obviously, this is too long for a competitive chip production. However, how much could hypothetically be gained by an optimization of the procedure? The periodic pattern of the HARE chips makes it suitable for multi-beam machining. With a 6.2 μm focal diameter, a 24 × 24 beam pattern could be realized on an area smaller than 4 × 4 mm^2. Accordingly, this setup could reduce the processing time by a factor of 576, amounting to a mere 1 min per chip. While these processing times appear highly competitive, another question pertains to the costs of the setup. A multi-beam setup as described above would require a 360 μJ pulse energy at 100 kHz, for which suitable lasers are commercially available. Based on current cost estimates, this would amount to approximately 320,000 € (Table S1). In addition to the initial investment, the material as well as power and maintenance costs have to be taken into consideration. The total electrical power consumption for the current setup comprising laser source, chiller, suction system, and axis system are approximately 3–3.5 kW. After 5,000 to 7,000 h of operation, the UV conversion module in the laser also needs to be replaced. Material costs for chips are therefore estimated at 2.33 cents. While profit estimations would be highly speculative regarding demand and other production overheads, we argue that the large capital investment is not necessarily prohibitive. Furthermore, once in place, such a setup would also enable the comparably convenient generation of prototypes, which allows for quickly testing different designs prior to mass production based on this or other technologies.

Wide adoption of serial crystallography has been limited in part due to the specialized methods and equipment required. As more X-ray sources adopt this approach, we anticipate greater emphasis on standardizing the most successful methods, which, due to their versatility and frugal sample consumption, will likely include fixed targets. Cheap and versatile chips are an important aspect during this process, particularly for making the technique more readily available. Cheap chips could be purchased as a consumable and used in a similar way to how SPINE mounts are used for rotation crystallography today. This promises to permit experimenters to prepare samples ahead of time and to focus on data collection during the beamtime, allow researchers to become more familiar with sample handling procedures, and facilitate remote serial data collections with pre-mounted samples.

EXPERIMENTAL PROCEDURES
Resource availability
Lead contact
Requests for further information and resources and reagents should be directed to and will be fulfilled by the lead contact, Eike C. Schulz (ec.schulz@uke.de).

Materials availability
This study did not generate new unique reagents.

Data and code availability
Any additional information required to reanalyze the data reported in this paper is either available from the stated database entries or from the lead contact upon request. No new code was generated in this study.

Laser drilling of the Kapton-based HARE chips

Polymer-based HARE chips were manufactured from off-the-shelf Kapton foils with thicknesses of 50 (DuPont) and 125 μm (Upilex), respectively. Films were mounted in a mechanical tensioning frame to create a flat processing surface with minimal wrinkles. Laser ablation was carried out with an Edgewave FX-100-2-GF USP laser mounted to the ILT UV-microscanner setup, as reported previously.[32] Utilizing the laser's third harmonic gave a 343 nm wavelength with a 1 ps pulse duration. The UV-microscanner was set to produce a 6.2 μm focus diameter ($1/e^2$). Systematic variations of the process parameter protocols were developed to remove 1 and μm per ablation layer for the 50 μm Kapton and 125 μm Kapton, respectively. After the ablation of each layer, the focal plane was repositioned accordingly. The truncated pyramidal wells were created using a crosshatch laser scanning pattern (Figure 1A) comprising 42 and 60 layers for the 50 μm and 125 μm chips, respectively. Finally, 10 repeated laser pulses were used to percussion drill a round exit hole for the feature aperture. A single HARE chip for each Kapton thickness was produced as a prototype for subsequent crystallographic evaluation and used throughout this study.

Confocal and light microscopy measurements

The results of the laser ablation were visualized on a Keyence VHX-7000 light microscope. Confocal measurements were taken on a Keyencee VK-9700. Confocal microscopy profiles for 20 features were extracted, and the feature widths were assessed by visual inspection. Each feature was fitted with a simple parabola to find the feature center, from which the distance between feature centers was calculated. Light microscopic images of protein microcrystals were obtained in a C-chip disposable hemocytometer (NanoEntek), following a Bürker grid pattern. Each square in the hemocytometer depicted in Figure 2 has a length of 0.2 mm and a depth of 0.1 mm, which corresponds to a volume of 0.004 mm^3 or 0.004 μL.

Cleaning of the Kapton-based HARE chips

Cleaning of the Kapton chips followed the same procedure to silicon chips.[26] In brief, the chips were soaked in 1% tergazyme to remove clearly visible deposits. Lukewarm water was passed over the chips, followed by isopropanol to speed up drying. Visual inspection and light microscopy confirmed chip cleanliness.

Proteinase K crystallization

Lyophilized proteinase K from *Tritirachium album* was purchased from Sigma-Aldrich (P2308) and resuspended in 50 mM HEPES (pH 7.0) at 60 mg/mL. Microcrystals were obtained by mixing proteinase K solution with precipitant solution (1 M $NaNO_3$, 0.1 M sodium citrate [pH 6.5]) in a 5:1 ratio and left overnight at room temperature. Measurements showed that the crystals were approximately 50 × 50 × 40 μm in size.

Thaumatin crystallization

Thaumatin from *Thaumatococcus daniellii* was purchased from Sigma-Aldrich (T7638) and crystallized as previously reported.[39] In brief, thaumatin was resuspended in 0.1 M potassium phosphate (pH 6.5) at 30 mg/mL. Microcrystals were formed via mixing protein solution with precipitant solution (0.1 M potassium phosphate [pH 6.5], 1.7 M potassium sodium tartrate) with a 1:3 ratio, respectively. Crystals grew at 20°C overnight and were measured to be approximately 25 × 10 × 10 μm.

CTX-M-14 crystallization

CTX-M-14 was purified as previously.[40] For crystallization, the CTX-M-14 solution (22 mg/mL) was mixed with a 45% (v/v) crystallizing agent (40% [m/v] PEG8000,

200 mM lithium sulfate, 100 mM sodium acetate [pH 4.5]) and a 5% (v/v) undiluted seed stock solution. Crystals with a homogeneous size distribution of 11–15 μm were obtained after approximately 90 min. Crystals were centrifuged at 200 × *g* for 5 min, and the supernatant was replaced with a stabilization buffer (28% [m/v] PEG8000, 140 mM lithium sulfate, 70 mM sodium acetate, 6 mM MES, 15 mM sodium chloride [pH 4.5]) to stop further crystal growth. Measurements showed that the crystals were approximately 15 × 15 × 15 μm in size.

Lysozyme crystallization

Lysozyme was purchased from Sigma-Aldrich (L6876). Crystals were prepared as described previously.[16] Briefly, for batch crystallization, lysozyme (67 mg/mL) was dissolved into buffer (20 mM sodium acetate [pH 4.7], 50 mM NaCl), and an equal amount of 1.7 M NaCl was added. Crystals grew immediately to an approximate size of 44 × 44 × 44 μm.

Tryptophan synthase crystallization

TrpA and TrpB were expressed and purified following previously established procedures.[41,42] The purified tryptophan synthase complex underwent batch micro-crystallization through incubation with the tryptophan synthase crystallization buffer conditions (20% [w/v] polyethylene glycol 300, 0.1 M Tris-HCl [pH 7.5], and 20 mM cesium chloride). The incubation led to the successful formation of oblong micro-crystals with approximate dimensions of 40 × 8 × 6 μm.

Sample loading in the Kapton-based HARE chips

Chips were loaded with 80–100 μL microcrystal slurry. Mother liquor was removed from the samples by applying a gentle suction force. Residual excess liquid on the opposite side of the chip from loading was removed via blotting. The loaded chips were kept in a humidified environment during sample loading. Serial datasets were collected for each sample from two Kapton chips with varying thickness (50 and 125 μm) and a standard silicon chip. Each dataset comprised 3 chip measurements to increase the total crystals for each dataset and assess the variation from the chip loading procedure, which followed the previously reported protocol.[26] Chips were aligned using the previously reported alignment procedure.[26]

Serial crystallography

All serial crystallography datasets were collected at the P14-2 endstation (T-REXX) of PETRA-III (DESY) at the EMBL Hamburg unit. Data were collected on an Eiger2M detector at an energy of 12.7 keV. The beam was focused to 10 × 10 μm with a flux 1.1 × 10^{12} ph/s. Samples were rastered across the X-ray beam at 30 Hz with 5 ms exposure except for tryptophan synthase, which was exposed for 8 ms. Diffraction quality was monitored live using DOZOR[43] analysis and ADXV.[44] Data processing was carried out with the CrystFEL software package.[45] Diffraction images where indexed and integrated using indexamajig, with the following options: –multi –peaks = zaef –threshold = 20 –min-gradient = 100 –min-snr = 5 –indexing = xgandalf –int-radius = 3,4,5. Reflection intensities were scaled and merged in partialator, with the following options: –max-overall, there = 65000 –iterations = 1 –model = unity.

Data processing

The structures were solved by molecular replacement using PHASER[46] and previously determined structures of lysozyme, thaumatin, proteinase K, CTX-M-14, and tryptophan synthase as search models (PDB: 3WUN, 2A7I, 1IC6, 6GTH, and 8B03, respectively). The structures were refined via iterative cycles of phenix.refine[47,48]

and manual model correction in COOT.[49,50] Protein structure and electron density images were generated in PyMOL.[51]

Scattering measurements on other polymers

Small sections from both types of Kapton chips, 100 μm COC, 12 μm COC, and 2.5 μm mylar, respectively, were cut into millimeter-by-millimeter sections. These were mounted onto pin mounts at the PETRA-III P13 beamline at the EMBL Hamburg unit. The beam was focused to 15 × 15 μm and a flux 4.5×10^{11} ph/s. The small sample pieces where aligned analogously to a single crystal, with the thinnest dimension orthogonal to the beam. Intensities were averaged over 10 s at 100% transmission. Images were combined and a radial average generated using the image_average and radial_average functions of dxtbx, part of the general cxtbx toolbox, respectively.

SUPPLEMENTAL INFORMATION

Supplemental information can be found online at https://doi.org/10.1016/j.xcrp. 2024.101987.

AUTHOR CONTRIBUTIONS

R.B. prepared the protein crystals, performed data collection, analyzed the data, prepared the figures, and wrote the manuscript; A.P. and S.S. performed protein expression, purification, crystallization, and data collection; L.v.S., S.D., and K.B. prepared the protein crystals and performed data collection; D.v.S and P.M. performed data collection and analyzed the data; M.B., G.L., B.S., and M.O. performed laser drilling experiments to make the Kapton HARE chips; M.W. provided resources for the research; E.C.S. designed the experiment, performed data collection, analyzed the data and wrote the manuscript; and all authors discussed and corrected the manuscript.

DECLARATION OF INTERESTS

The authors declare no competing interests.

REFERENCES

1. Pearson, A.R., and Mehrabi, P. (2020). Serial synchrotron crystallography for time-resolved structural biology. Curr. Opin. Struct. Biol. 65, 168–174. https://doi.org/10.1016/j.sbi.2020. 06.019.

2. Barends, T.R.M., Stauch, B., Cherezov, V., and Schlichting, I. (2022). Serial femtosecond crystallography. Nat. Rev. Methods Primers 2, 59. https://doi.org/10.1038/s43586-022-00141-7.

3. Chapman, H.N., Fromme, P., Barty, A., White, T.A., Kirian, R.A., Aquila, A., Hunter, M.S., Schulz, J., DePonte, D.P., Weierstall, U., et al. (2011). Femtosecond X-ray protein nanocrystallography. Nature

470, 73–77. https://doi.org/10.1038/nature09750.

4. Stellato, F., Oberthür, D., Liang, M., Bean, R., Gati, C., Yefanov, O., Barty, A., Burkhardt, A., Fischer, P., Galli, L., et al. (2014). Room-temperature macromolecular serial crystallography using synchrotron radiation. IUCrJ *1*, 204–212. https://doi.org/10.1107/S2052252514010070.

5. Chapman, H.N. (2019). X-ray free-electron lasers for the structure and dynamics of macromolecules. Annu. Rev. Biochem. *88*, 35–58. https://doi.org/10.1146/annurev-biochem-013118-110744.

6. Ebrahim, A., Appleby, M.V., Axford, D., Beale, J., Moreno-Chicano, T., Sherrell, D.A., Strange, R.W., Hough, M.A., and Owen, R.L. (2019a). Resolving polymorphs and radiation-driven effects in microcrystals using fixed-target serial synchrotron crystallography. Acta Crystallogr. D *75*, 151–159. https://doi.org/10.1107/S2059798318010240.

7. Mehrabi, P., Bücker, R., Bourenkov, G., Ginn, H.M., von Stetten, D., Müller-Werkmeister, H.M., Kuo, A., Morizumi, T., Eger, B.T., Ou, W.L., et al. (2021a). Serial femtosecond and serial synchrotron crystallography can yield data of equivalent quality: A systematic comparison. Sci. Adv. *7*, eabf1380. https://doi.org/10.1126/sciadv.abf138.

8. Mehrabi, P., von Stetten, D., Leimkohl, J.P., Tellkamp, F., and Schulz, E.C. (2021b). An environmental control box for serial crystallography enables multi-dimensional experiments. bioRxiv, 2011–20121doi. https://doi.org/10.1101/2021.11.07.467596.

9. Weinert, T., Skopintsev, P., James, D., Dworkowski, F., Panepucci, E., Kekilli, D., Furrer, A., Brünle, S., Mous, S., Ozerov, D., et al. (2019). Proton uptake mechanism in bacteriorhodopsin captured by serial synchrotron crystallography. Science *365*, 61–65. https://doi.org/10.1126/science.aaw86.

10. Mehrabi, P., Schulz, E.C., Dsouza, R., Müller-Werkmeister, H.M., Tellkamp, F., Miller, R.J.D., and Pai, E.F. (2019b). Time-resolved crystallography reveals allosteric communication aligned with molecular breathing. Science *365*, 1167–1170. https://doi.org/10.1126/science.aaw9904.

11. Schulz, E.C., Yorke, B.A., Pearson, A.R., and Mehrabi, P. (2022). Best practices for time-resolved serial synchrotron crystallography. Acta Crystallogr. D *78*, 14–29. https://doi.org/10.1107/S2059798321011621.

12. Weierstall, U., Spence, J.C.H., and Doak, R.B. (2012). Injector for scattering measurements on fully solvated biospecies. Rev. Sci. Instrum. *83*, 035108. https://doi.org/10.1063/1.3693040.

13. Butryn, A., Simon, P.S., Aller, P., Hinchliffe, P., Massad, R.N., Leen, G., Tooke, C.L., Bogacz, I., Kim, I.S., Bhowmick, A., et al. (2021). An on-demand, drop-on-drop method for studying enzyme catalysis by serial crystallography. Nat. Commun. *12*, 4461. https://doi.org/10.1038/s41467-021-24757-7.

14. Martiel, I., Müller-Werkmeister, H.M., and Cohen, A.E. (2019). Strategies for sample delivery for femtosecond crystallography. Acta Crystallogr. D *75*, 160–177. https://doi.org/10.1107/S2059798318017953.

15. Schulz, E.C., Mehrabi, P., Müller-Werkmeister, H.M., Tellkamp, F., Jha, A., Stuart, W., Persch, E., De Gasparo, R., Diederich, F., Pai, E.F., and Miller, R.J.D. (2018). The hit-and-return system enables efficient time-resolved serial synchrotron crystallography. Nat. Methods *15*, 901–904. https://doi.org/10.1038/s41592-018-0180-2.

16. Mehrabi, P., Schulz, E.C., Agthe, M., Horrell, S., Bourenkov, G., von Stetten, D., Leimkohl, J.P., Schikora, H., Schneider, T.R., Pearson, A.R., et al. (2019a). Liquid application method for time-resolved analyses by serial synchrotron crystallography. Nat. Methods *16*, 979–982. https://doi.org/10.1038/s41592-019-0553-1.

17. Gati, C., Bourenkov, G., Klinge, M., Rehders, D., Stellato, F., Oberthür, D., Yefanov, O., Sommer, B.P., Mogk, S., Duszenko, M., et al. (2014). Serial crystallography on in vivo grown microcrystals using synchrotron radiation. IUCrJ *1*, 87–94. https://doi.org/10.1107/S2052252513033939.

18. Hirata, K., Shinzawa-Itoh, K., Yano, N., Takemura, S., Kato, K., Hatanaka, M., Muramoto, K., Kawahara, T., Tsukihara, T., Yamashita, E., et al. (2014). Determination of damage-free crystal structure of an X-ray–sensitive protein using an XFEL. Nat. Methods *11*, 734–736. https://doi.org/10.1038/nmeth.2962.

19. Doak, R.B., Nass Kovacs, G., Gorel, A., Foucar, L., Barends, T.R.M., Grünbein, M.L., Hilpert, M., Kloos, M., Roome, C.M., Shoeman, R.L., et al. (2018). Crystallography on a chip – without the chip: Sheet-on-sheet sandwich. Acta Crystallogr. D *74*, 1000–1007. https://doi.org/10.1107/S2059798318011634.

20. Roedig, P., Duman, R., Sanchez-Weatherby, J., Vartiainen, I., Burkhardt, A., Warmer, M., David, C., Wagner, A., and Meents, A. (2016). Room-temperature macromolecular crystallography using a micro-patterned silicon chip with minimal background scattering. J. Appl. Crystallogr. *49*, 968–975. https://doi.org/10.1107/S1600576716006348.

21. Roedig, P., Vartiainen, I., Duman, R., Panneerselvam, S., Stübe, N., Lorbeer, O., Warmer, M., Sutton, G., Stuart, D.I., Weckert, E., et al. (2015). A micro-patterned silicon chip as sample holder for macromolecular crystallography experiments with minimal background scattering. Sci. Rep. *5*, 10451. https://doi.org/10.1038/srep10451.

22. Oghbaey, S., Sarracini, A., Ginn, H.M., Pare-Labrosse, O., Kuo, A., Marx, A., Epp, S.W., Sherrell, D.A., Eger, B.T., Zhong, Y., et al. (2016). Fixed target combined with spectral mapping: Approaching 100% hit rates for serial crystallography. Acta Crystallogr. D *72*, 944–955. https://doi.org/10.1107/S2059798316010834.

23. Mueller, C., Marx, A., Epp, S.W., Zhong, Y., Kuo, A., Balo, A.R., Soman, J., Schotte, F., Lemke, H.T., Owen, R.L., et al. (2015). Fixed target matrix for femtosecond time-resolved and in situ serial micro-crystallography. Struct. Dyn. *2*, 054302. https://doi.org/10.1063/1.4928706.

24. Sherrell, D.A., Foster, A.J., Hudson, L., Nutter, B., O'Hea, J., Nelson, S., Paré-Labrosse, O., Oghbaey, S., Miller, R.J.D., and Owen, R.L. (2015). A modular and compact portable mini-endstation for high-precision, high-speed fixed target serial crystallography at FEL and synchrotron sources. J. Synchrotron Radiat. *22*, 1372–1378. https://doi.org/10.1107/S1600577515016938.

25. Roedig, P., Ginn, H.M., Pakendorf, T., Sutton, G., Harlos, K., Walter, T.S., Meyer, J., Fischer, P., Duman, R., Vartiainen, I., et al. (2017). High-speed fixed-target serial virus crystallography. Nat. Methods *14*, 805–810. https://doi.org/10.1038/nmeth.4335.

26. Mehrabi, P., Müller-Werkmeister, H.M., Leimkohl, J.P., Schikora, H., Ninkovic, J., Krivokuca, S., Andriček, L., Epp, S.W., Sherrell, D., Owen, R.L., et al. (2020). The HARE chip for efficient time-resolved serial synchrotron crystallography. J. Synchrotron Radiat. *27*, 360–370. https://doi.org/10.1107/S1600577520000685.

27. Lee, D., Baek, S., Park, J., Lee, K., Kim, J., Lee, S.J., Chung, W.K., Lee, J.L., Cho, Y., and Nam, K.H. (2019). Nylon mesh-based sample holder for fixed-target serial femtosecond crystallography. Sci. Rep. *9*, 6971. https://doi.org/10.1038/s41598-019-43485-z.

28. Zarrine-Afsar, A., Barends, T.R.M., Müller, C., Fuchs, M.R., Lomb, L., Schlichting, I., and Miller, R.J.D. (2012). Crystallography on a chip. Acta Crystallogr. D *68*, 321–323. https://doi.org/10.1107/S0907444911055296.

29. Carrillo, M., Mason, T.J., Karpik, A., Martiel, I., Kepa, M.W., McAuley, K.E., Beale, J.H., and Padeste, C. (2023). Micro-structured polymer fixed targets for serial crystallography at synchrotrons and xfels. IUCrJ *10*, 678–693. https://doi.org/10.1107/S2052252523007595.

30. Ebrahim, A., Moreno-Chicano, T., Appleby, M.V., Chaplin, A.K., Beale, J.H., Sherrell, D.A., Duyvesteyn, H.M.E., Owada, S., Tono, K., Sugimoto, H., et al. (2019b). Dose-resolved serial synchrotron and XFEL structures of radiation-sensitive metalloproteins. IUCrJ *6*, 543–551. https://doi.org/10.1107/S2052252519003956.

31. Bar-Even, A., Noor, E., Savir, Y., Liebermeister, W., Davidi, D., Tawfik, D.S., and Milo, R. (2011). The moderately efficient enzyme: evolutionary and physicochemical trends shaping enzyme parameters. Biochemistry *50*, 4402–4410. https://doi.org/10.1021/bi2002289.

32. Danylyuk, S., Osbild, M., Korr, L., Fischer, M., Delmdahl, R., and Reininghaus, M. (2023). Sub-micrometer structuring of surfaces with deep UV lasers. Laser-Based Micro- and Nanoprocessing *XVII*, 183–192. https://doi.org/10.1117/12.2647865.

33. Wilson, M.A. (2022). Mapping enzyme landscapes by time-resolved crystallography with synchrotron and x-ray free electron laser light. Annu. Rev. Biophys. *51*, 79–98. https://doi.org/10.1146/annurev-biophys-100421-110959.

34. Axford, D., Aller, P., Sanchez-Weatherby, J., and Sandy, J. (2016). Applications of thin-film sandwich crystallization platforms. Acta Crystallogr. F *72*, 313–319. https://doi.org/10.1107/S2053230X16004386.

35. Broecker, J., Klingel, V., Ou, W.L., Balo, A.R., Kissick, D.J., Ogata, C.M., Kuo, A., and Ernst, O.P. (2016). A Versatile System for High-Throughput In Situ X-ray Screening and Data Collection of Soluble and Membrane-Protein Crystals. Cryst. Growth Des. *16*, 6318–6326. https://doi.org/10.1021/acs.cgd.6b00950.

36. Gilbile, D., Shelby, M.L., Lyubimov, A.Y., Wierman, J.L., Monteiro, D.C.F., Cohen, A.E., Russi, S., Coleman, M.A., Frank, M., and Kuhl, T.L. (2021). Plug-and-play polymer microfluidic chips for hydrated, room temperature, fixed-target serial crystallography. Lab Chip *21*, 4831–4845. https://doi.org/10.1039/d1lc00810b.

37. Illava, G., Jayne, R., Finke, A.D., Closs, D., Zeng, W., Milano, S.K., Huang, Q., Kriksunov, I., Sidorenko, P., Wise, F.W., et al. (2021). Integrated sample-handling and mounting system for fixed-target serial synchrotron crystallography. Acta Crystallogr. D *77*, 628–644. https://doi.org/10.1107/S2059798321001868.

38. Gotthard, G., Flores-Ibarra, A., Carrillo, M., Kepa, M.W., Mason, T.J., Stegmann, D.P., Olasz, B., Pachota, M., Dworkowski, F., Ozerov, D., et al. (2023). Fixed-target time-resolved crystallography at xfels: the scourge of light contamination but reduced sample consumption. Preprint at bioRxiv. https://doi.org/10.1101/2023.12.12.571218.

39. Guo, G., Fuchs, M.R., Shi, W., Skinner, J., Berman, E., Ogata, C.M., Hendrickson, W.A., McSweeney, S., and Liu, Q. (2018). Sample manipulation and data assembly for robust microcrystal synchrotron crystallography. IUCrJ *5*, 238–246. https://doi.org/10.1107/S2052252518005389.

40. Wiedorn, M.O., Oberthür, D., Bean, R., Schubert, R., Werner, N., Abbey, B., Aepfelbacher, M., Adriano, L., Allahgholi, A., Al-Qudami, N., et al. (2018). Megahertz serial crystallography. Nat. Commun. *9*, 4025. https://doi.org/10.1038/s41467-018-06156-7.

41. Mehrabi, P., Sung, S., von Stetten, D., Prester, A., Hatton, C.E., Kleine-Döpke, S., Berkes, A., Gore, G., Leimkohl, J.P., Schikora, H., et al. (2023). Millisecond cryo-trapping by the spitrobot crystal plunger simplifies time-resolved crystallography. Nat. Commun. *14*, 2365. https://doi.org/10.1038/s41467-023-37834-w.

42. Kneuttinger, A.C., Zwisele, S., Straub, K., Bruckmann, A., Busch, F., Kinateder, T., Gaim, B., Wysocki, V.H., Merkl, R., and Sterner, R. (2019). Light-regulation of tryptophan synthase by combining protein design and enzymology. Int. J. Mol. Sci. *20*, 5106. https://doi.org/10.3390/ijms20205106.

43. Zander, U., Bourenkov, G., Popov, A.N., de Sanctis, D., Svensson, O., McCarthy, A.A., Round, E., Gordeliy, V., Mueller-Dieckmann, C., and Leonard, G.A. (2015). MeshAndCollect: An automated multi-crystal data-collection workflow for synchrotron macromolecular crystallography beamlines. Acta Crystallogr. D *71*, 2328–2343. https://doi.org/10.1107/S1399004715017927.

44. Arvai, A. (2012). Adxv—a Program to Display X-Ray Diffraction Images (Scripps Research Institute: La Jolla).

45. White, T.A., Kirian, R.A., Martin, A.V., Aquila, A., Nass, K., Barty, A., and Chapman, H.N. (2012). Crystfel: a software suite for snapshot serial crystallography. J. Appl. Crystallogr. *45*, 335–341. https://doi.org/10.1107/S0021889812002312.

46. McCoy, A.J., Grosse-Kunstleve, R.W., Adams, P.D., Winn, M.D., Storoni, L.C., and Read, R.J. (2007). Phaser crystallographic software. J. Appl. Crystallogr. *40*, 658–674. https://doi.org/10.1107/S0021889807021206.

47. Adams, P.D., Gopal, K., Grosse-Kunstleve, R.W., Hung, L.W., Ioerger, T.R., McCoy, A.J., Moriarty, N.W., Pai, R.K., Read, R.J., Romo, T.D., et al. (2004). Recent developments in the phenix software for automated crystallographic structure determination. J. Synchrotron Radiat. *11*, 53–55. https://doi.org/10.1107/s0909049503024130.

48. Liebschner, D., Afonine, P.V., Moriarty, N.W., Poon, B.K., Sobolev, O.V., Terwilliger, T.C., and Adams, P.D. (2017). Polder maps: improving omit maps by excluding bulk solvent. Acta Crystallogr. D *73*, 148–157. https://doi.org/10.1107/S2059798316018210.

49. Emsley, P., and Cowtan, K. (2004). Coot: model-building tools for molecular graphics. Acta Crystallogr. D *60*, 2126–2132. https://doi.org/10.1107/S0907444904019158.

50. Emsley, P., Lohkamp, B., Scott, W.G., and Cowtan, K. (2010). Features and development of coot. Acta Crystallogr. D *66*, 486–501. https://doi.org/10.1107/S0907444910007493.

51. Schrodinger, L. (2015). The Pymol Molecular Graphics System. Version 1, 8.